Three-Dimensional Heat Transfer Analysis of Laser-Arc Hybrid Welding Process

T. Mukherjee and A. De*
[1]Mechanical Engineering Department, Indian Institute of Technology Bombay, Mumbai – 400076
*Communicating author E-mail: amit@iitb.ac.in)

ABSTRACT

Laser-arc hybrid welding process employs a laser beam and a welding arc concurrently for the joining of thick plates at high welding speeds. Systematic quantitative studies to understand the role of welding conditions on the rate of heat input and weld pool profile are important but rarely reported for hybrid welding process. The current work presents a three-dimensional heat transfer analysis of hybrid welding process using finite element method. The computed results are validated using experimentally measured results that are reported in the independent literature. The model is used further to examine the effect of welding speed, laser and arc power, and the separation distance between laser beam and welding arc on the weld pool profile. The computed results show that the weld width will reduce with increase in welding speed and the separation distance while the penetration increases with the laser power.

KEY WORDS : Laser-arc hybrid welding, Numerical model, Heat transfer analysis, Weld pool profile

1.0 INTRODUCTION

Laser-arc hybrid welding process involves simultaneous application of a laser beam and an electrical arc. As a result, the hybrid welding provides a greater rate of heat input in comparison to either laser beam welding (LBW) or a conventional gas tungsten arc (GTA) or gas metal arc (GMA) welding process. Increased gap tolerances and melting efficiency, high welding speed, and reduced weld cracking, porosity, and evaporation loss of alloying elements are some of the major benefits of the hybrid welding process [1–4]. However, an accurate control of the welding conditions is needed in hybrid welding due to the presence of two heat sources and their combined effect on the rate of heat input. For example, a higher laser beam power in comparison to the arc power could lead to greater cooling rate and weld joint hardness [5]. In contrast, higher arc power compared to that of the laser beam could inhibit the formation of laser induced keyhole and reduce the weld penetration [6]. Increase in the separation distance between the laser beam and the arc also reduces the melting efficiency and penetration but increases the cooling rate [1, 2, 6–9]. The final profile and the structure of the weld is significantly affected by the rate of heat input per unit length. The main purpose of the present work is therefore to probe the effect of the key welding conditions on the rate of heat input and final weld pool profiles through a comprehensive heat transfer analysis in laser-arc hybrid welding process.

In recent times, several efforts are reported to simulate laser-arc hybrid welding process using either heat conduction [10-14] or convective [2, 15-17] heat transfer based models. Although these models [2, 10-17] helped to understand several physical processes involved in the hybrid welding process, quantitative studies of the role of welding conditions on weld pool profiles are needed and still evolving. We present here a three-dimensional heat transfer analysis of a typical laser–GTA hybrid welding process using finite element method.

A novel methodology is adapted to account for the heat input due to laser beam through a volumetric source term while the heat input due to welding arc is considered as a surface heat flux. The computed weld pool profiles are checked with the corresponding experimentally measured welds that are reported in independent literature. Next, the model is used to examine the effect of several key process variables on the temperature distribution and pool profiles in laser-gas tungsten arc hybrid welding.

2.0 THEORETICAL FORMULATION

A three-dimensional (3D) pseudo-steady state heat transfer analysis is conducted to simulate the temperature field in laser-GTA hybrid welding process. The governing heat conduction equation can be stated as

$$\frac{\partial}{\partial \xi}\left(k\frac{\partial T}{\partial \xi}\right)+\frac{\partial}{\partial y}\left(k\frac{\partial T}{\partial y}\right)+\frac{\partial}{\partial z}\left(k\frac{\partial T}{\partial z}\right)+\dot{Q} = -\rho C v_w \frac{\partial T}{\partial \xi} \quad \text{..... (1)}$$

where ρ, k and C are the density, thermal conductivity and specific heat of workpiece material, T is the temperature variable, V_w is the constant welding speed, $\dot{Q}$ is the rate of internal heat generation, and $\xi = x - v_w t$ that depicts the distance of a point from the center of the moving heat source (welding arc / laser beam) at any time t in the direction of welding speed. The boundary conditions are considered as

$$k\frac{\partial T}{\partial n} - q + h(T - T_0) + \sigma\varepsilon(T^4 - T_0^4) = 0 \quad \text{..... (2)}$$

where h is the surface heat transfer coefficient, q is the input heat flux due to welding heat source, and ϵ, σ and T_0 are the emissivity, Stefan-Boltzman constant, and the surrounding temperature, respectively.

Fig.1 schematically shows the solution domain and the boundary conditions. A lumped heat transfer coefficient, h, is considered to account for both the convection and radiation heat losses as $h = 2.4 \times 10^{-3} \times \epsilon \times T^{1.61}$ [18]. The heat flux, q, due to the welding arc follows a Gaussian distribution as

$$q = \frac{d\eta_a P_a}{\pi r_a^2}\exp\left(\frac{-dr^2}{r_a^2}\right) \quad \text{..... (3)}$$

where P_a is the nominal arc power, ha is the arc efficiency, d is arc energy distribution factor and r_a is the effective arc radius on the top surface of the workpiece.

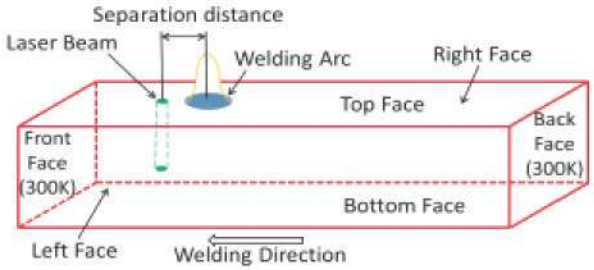

Fig. 1 : Schematic diagram of the solution domain and applied boundary conditions

The heat input due to the laser beam is considered through a volumetric source term, $\dot{q}$, as

$$\dot{q} = q_0 \exp\left[\frac{-3r^2}{r_\ell^2(z)}\right] \quad \text{..... (4)}$$

where, $r_\ell(z) = r_1 - \frac{(r_1 - r_2)\times z}{z_2}$ ..... (5)

where r_1 and r_2 are the maximum and the minimum radii of the source respectively at the top surface and at a depth z_2, and $r_\ell(z)$ is the source radius at any depth z from the top surface. The term r_1 is considered as the focused beam radius at the top surface. The term q_0 is estimated as [18],

$$q_0 = \frac{9\eta_\ell P_\ell e^3}{\pi(e^3 - 1)} \times \frac{1}{z_2(r_1^2 + r_1 r_2 + r_2^2)} \quad \text{..... (6)}$$

where P_ℓ is the nominal beam power and η_ℓ is the absorption coefficient. Equations (4) – (6) show that a-priori estimation of r_2 and z_2 is needed to define $\dot{q}$ explicitly. A novel method is proposed here, as shown in Appendix-I, to estimate the values of r_2 and z_2 as function of the welding conditions only.

3.0 RESULTS AND DISCUSSIONS

The numerical model is used to simulate laser-GTA hybrid welding of a 10 mm thick A131 structural steel [2] and a 4 mm thick AISI 321 stainless steel [6]. **Table 1** shows the corresponding welding conditions as reported in references [2] and [6]. The thermophysical properties of these materials are taken from standard handbook.

The numerical model is tested first for its ability to predict the weld pool shapes in a reliable manner separately in GTAW and LBW processes. **Fig. 2** shows a comparison of the experimentally measured [2] and corresponding computed weld pool shape in GTAW of 4 mm thick A131 structural steel at welding current, voltage and speed of 190 A, 12.3 V and 8.5 mm/s, respectively. In the computed weld pool profile, the fusion zone is indicated by the red colored zone with the 1800 K isotherm as the boundary and the HAZ is the region bounded by 1100 K and 1400 K isotherms. **Fig. 3** shows a comparison of the computed and the corresponding measured weld pool shape in LBW of 4 mm thick A131 structural steel at a beam power of 4.5 kW and welding speed of 8.5 mm/s. A comparison of **Fig. 2** and **Fig. 3** shows that the laser beam results in a deeper melt pool while the GTAW process provides a wider and shallower weld pool. Overall, **Fig. 2** and **Fig. 3** show that the model can predict the weld pool shapes fairly well in GTA and laser beam welding processes.

Fig. 4(a) shows a three-dimensional view of the computed melt pool profile for laser-GTA hybrid welding in A131 structural steel of 10 mm thickness. A zoomed view of the melt pool profile is presented in **Fig. 4(b)** for clarity. The fusion zone is bounded by the 1800 K isotherm while the HAZ is presumed to be bounded by 1300 K and 1500 K isotherms. A deep penetration towards the front end of the pool attributes the effect of the leading laser beam. The wider and shallower melt pool at the rear side depicts the effect of the trailing welding arc.

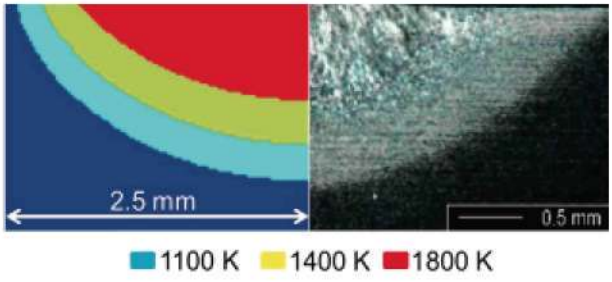

Fig. 2 : Comparison of computed and the corresponding measured weld pool in GTAW of 4 mm thick A131 steel at welding current, voltage and speed of 190 A, 12.3 V and 8.5 mm/s, respectively.

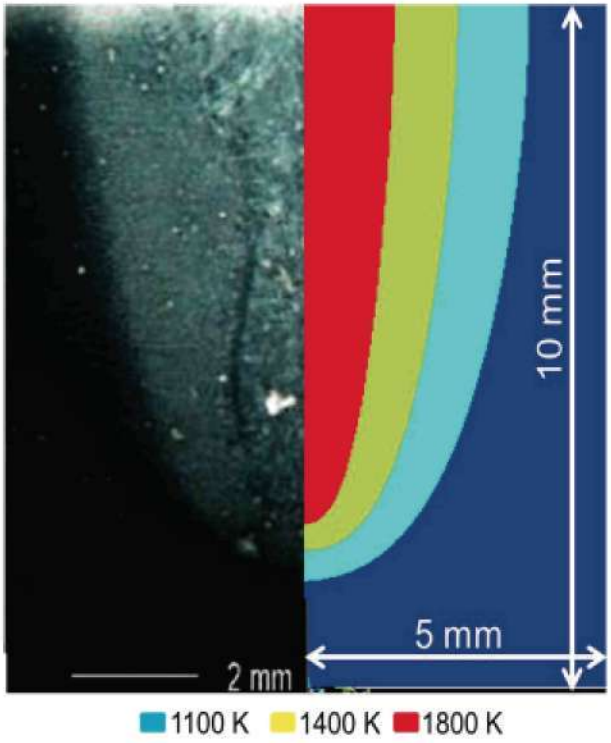

Fig. 3 : Comparison of computed and the corresponding measured weld pool in LBW of 4 mm thick A131 steel at a beam power of 4.5 kW and welding speed of 8.5 mm/s.

Fig. 4 indicates that the hybrid weld pool will be characterized by varying transverse cross-sections along the length of the weld due to the concurrent application of leading laser beam and trailing welding arc. **Figs. 5 (a)** to **(e)** present the computed transverse views of the weld pool along the six dotted sections indicated in **Fig. 4(b)**. **Fig. 5(a)** shows that a deep penetration is created under the laser beam. The effect of the leaser beam diminishes towards the rear of the pool as shown in **Figs. 5(b)** to **(d)**. The weld pool is at its widest below the welding arc as indicated in **Fig. 5(e)**. A comparison of **Figs 5(a)** to **(e)** also shows that the weld pool undergoes a minimum penetration along the length of the weld.

Figs. 6(a) to **(c)** show the computed and the corresponding measured hybrid weld pool profiles for three different welding conditions are in fair agreement. The model is used next to investigate the effect of different welding conditions on weld pool profile.

Figs. 7(a) and **(b)** show the computed melt pool profile for laser-GTA hybrid welding respectively with the laser beam and the welding arc as the lading sources. A comparison of **Figs 7(a)** and **(b)** show that the weld penetration is greater with the arc as the leading source that can be attributed to the preheating effect by the welding arc.

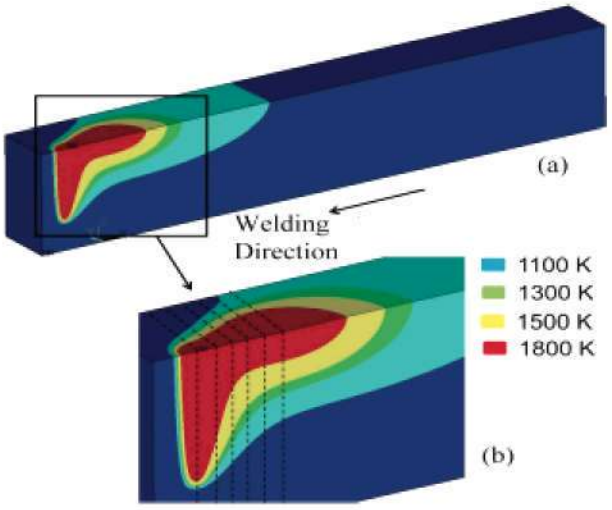

Fig. 4(a) : 3D isometric and (b) a zoomed view of computed weld pool shape in laser-GTA hybrid welding of 4 mm thick A131 steel. The welding conditions are in Table 1.

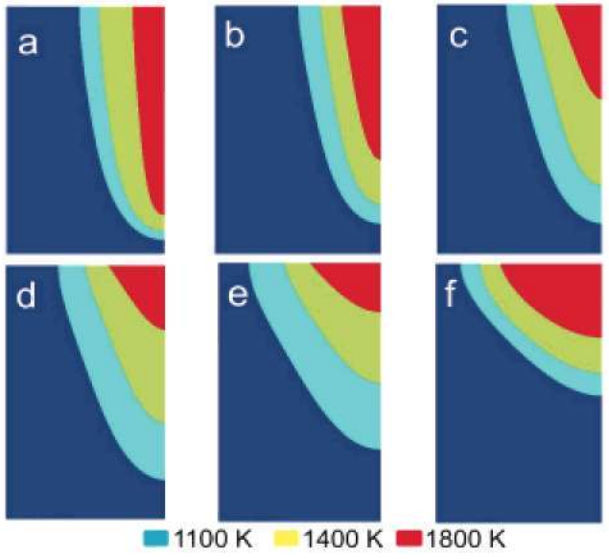

Fig. 5 : Computed transverse weld shapes at different cross-sections as indicated by the dotted lines in Fig. 4(b).

Figs. 8(a) to **(c)** show the effect of the laser beam power on the weld pool shape in laser-GTA hybrid welding of 10 mm thick A131 structural steel. With the increase of laser power more heat is supplied to the workpiece through the laser spot area. A comparison of **Figs. 8(a)** to **(c)** indicates that the weld penetration and the overall pool size increase significantly with increase in the laser beam power.

Figs. 9(a) to **(d)** show the effect of the separation distance between the laser beam and welding arc on the weld pool profiles at two different welding speeds. A comparison of **Figs 9(a)** and **(b)**, and of **Figs. 9(c)** and **(d)** shows that the increase in welding speed from 10 mm/s to 16 mm/s

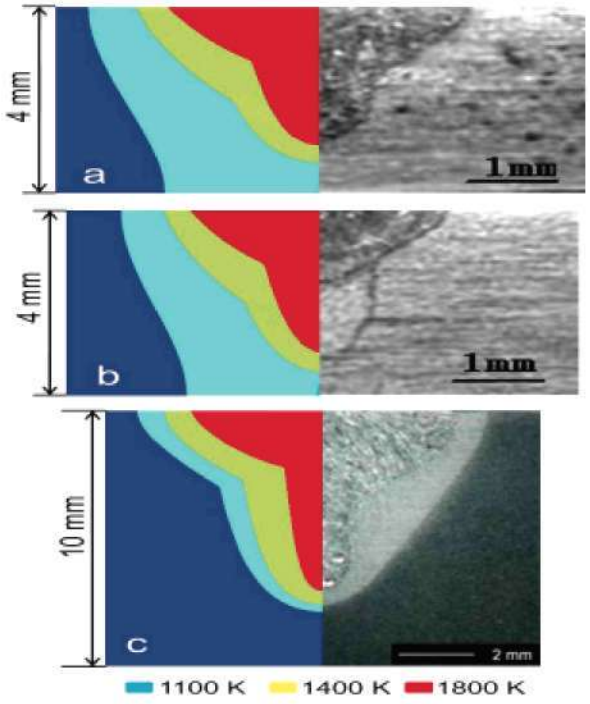

Fig. 6 : Comparison of computed and the corresponding measured weld pool shapes in laser-GTA hybrid welding at a constant welding current, voltage and speed of 120 A, 12 V and 1 mm/s, respectively. The laser beam power is (a) 1 kW, (b) 1.5 kW, and (c) 4.5 kW. The material is 4 mm thick AISI 321 for (a) & (b), and 10 mm thick A131 structural steel for (c).

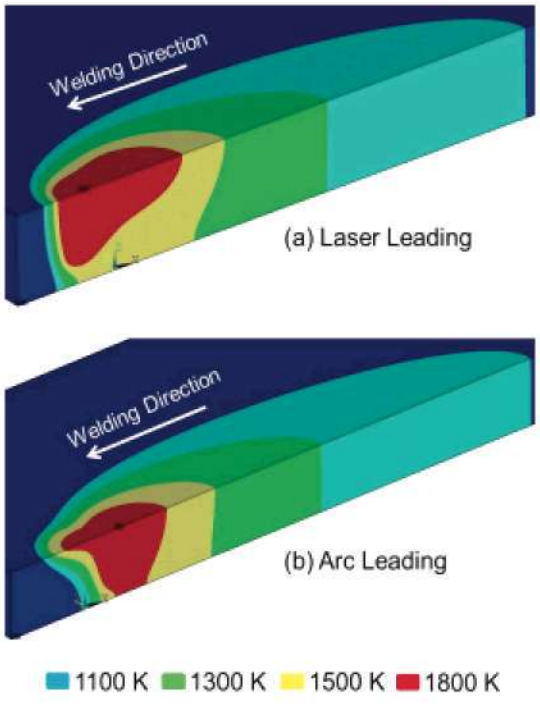

Fig. 7: Computed weld pool shapes with (a) laser beam leading and (b) welding arc leading in laser-GTA hybrid welding of 4 mm thick AISI321 steel. The welding conditions are in Table 1.

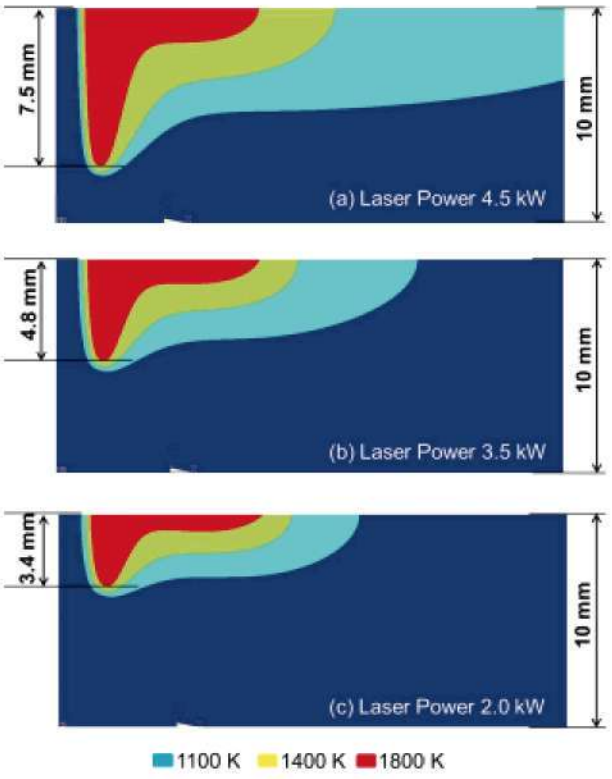

Fig. 8 : Influence of laser beam power on the computed hybrid weld pool shapes in 10 mm thick A131 structural steel. Laser powers are (a) 4.5 kW, (b) 3.5 kW and (c) 2.0 kW. Other welding conditions are in Table 1.

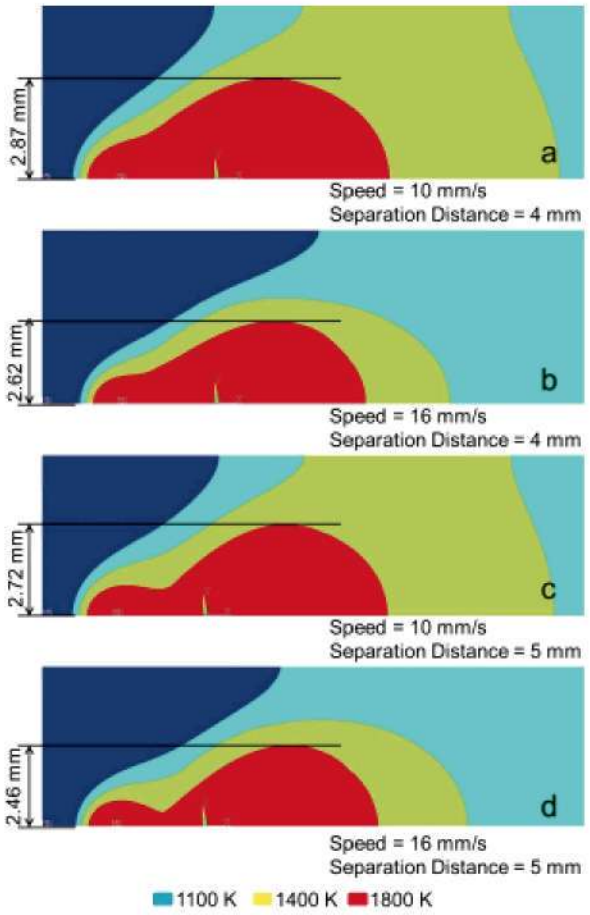

Fig. 9 : Influence of welding speed and source separation distance in laser-GTA hybrid welding of A131 structural steel. Welding conditions are in Table 1.

marginally reduces the weld width and the overall pool size on the top surface. In contrast, a comparison of **Figs 9(a)** and **(c)** and of **Figs 9(b)** and **(d)** depicts that the weld pool width reduces significantly with the increase in the separation distance between the laser beam and the welding arc. The effect of the separation distance is more pronounced at higher welding speed that is expected due to the reduced rate of overall heat input at higher welding speed. For a given welding condition, the weld pool created by the laser beam and the welding arc can be disintegrated at very high welding speed as shown in **Figs 10(a)** to **(d)**.

A three-dimensional heat transfer model to analyse laser-GTA hybrid welding is presented here. The computed results of weld pool shape are validated with the corresponding measured results reported in independent literature for hybrid welding as well as for GTAW and LBW, separately. The numerical model has been utilized further to show the effects of various key welding conditions on the weld pool shape in laser-GTA hybrid welding.

4.0 CONCLUSION

A novel approach is presented here to define a volumetric heat source term to account for the heat input from a high intensity laser beam using simple energy balance and considering only the welding conditions. The volumetric source term and a surface heat flux term are used to account for respectively the laser beam and the welding arc to develop the 3D heat transfer model for laser-GTA hybrid welding. The computed results show that the separation distance between the laser beam and the welding arc, and their respective position (leading / trailing) and the welding speed are the critical variables in laser-GTA hybrid welding. In particular, the weld pools created by the laser beam and the welding arc can go through a minimum penetration depth or get disintegrated for a gentle increase in the separation distance and at higher welding speeds with the beam and arc powers remaining the same.

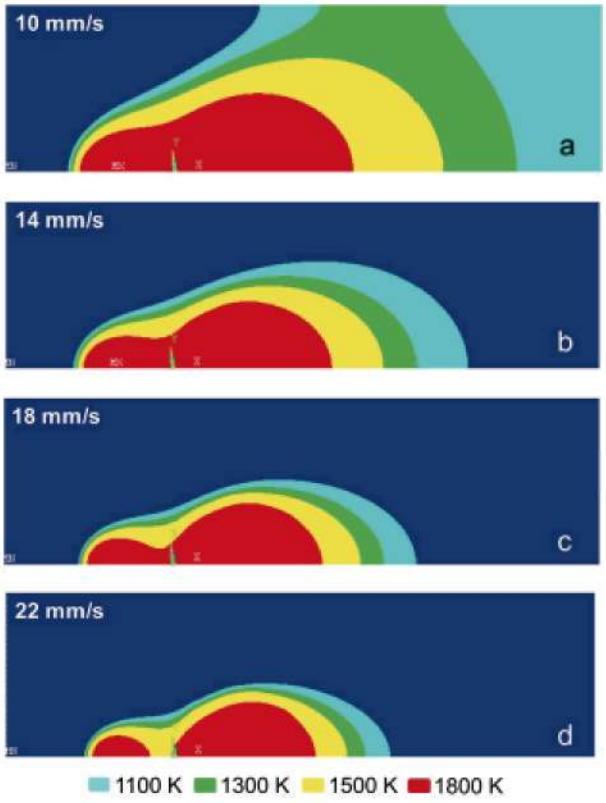

Fig. 10: Influence of very high welding speed on computed pool shapes in laser-GTA hybrid welding of A131 structural steel. Welding conditions are in Table 1.

REFERENCES

1. Ribic, B., Palmer, T. A. and Debroy, T. (2009); "Problems and issues in laser-arc hybrid welding", Int. Mater. Rev., 54 (4), 223–243.
2. Ribic, B., Rai, R. and Debroy, T. (2008); "Numerical simulation of heat transfer and fluid flow in GTA/Laser hybrid welding"; Sci. Technol. Weld. Joining, 13 (8), 683 – 693.
3. Hu, B. and Den Ouden, G. (2008); "Synergic effects of hybrid laser/arc welding", Sci. Technol. Weld. Joining, 13, (8), 683 – 693.
4. Cho, M. H., Farson, D. F., Lim, Y. C. and Choi, W. H. (2007); "Hybrid laser/arc welding processes for controlling bead profile", Sci. Technol. Weld. Joining, 12 (8), 677–688.
5. Gao, M., Zeng, X. Y., Hu, Q. W. and Yan, J. (2008); "Weld microstructure and shape of laser – arc hybrid welding", Sci. Technol. Weld. Joining, 13 (2), 106–113.
6. Chen, Y. B., Lei, Z. L., Li, Q. L. and Wu, L. (2006); "Experimental study on welding characteristics of CO_2 laser TIG hybrid welding process", Sci. Technol. Weld. Joining, 11 (4), 403–411.
7. Huang, R. S., Liu, L. M. and Song, G. (2007); "Infrared temperature measurement and interference analysis of magnesium alloys in hybrid laser-TIG welding process", Mater. Sc. Eng. A, 447 (½), 239–244.
8. Liu, L.M., Song, G. and Zhu, M.L. (2008); "Low-power laser/arc hybrid welding behavior in AZ-based Mg alloys", Metall. Mater. Trans. A, 39A (7), 1702–1711.
9. Liu, L. M., Yuan, S. T. and Li, C. B. (2012); "Effect of relative location of laser beam and TIC arc in different hybrid welding modes", Sci. Technol. Weld. Joining, 17 (6), 441–446.
10. Chen, Y. B., Li, L. Q., Fang, J. F. and Fang, X. S. (2003); "Numerical analysis of energy effect in laser-TIG hybrid welding", J. Mater. Sci. Technol., 19 (1), 23–26.
11. Xu, P. Q., Bao, C. M., Lu, F. G., Ma, C. W., He, J. P., Cui, H. C. and Yang, S. L. (2011); "Numerical simulation of laser-tungsten inert arc deep penetration welding between WC-Co cemented carbide and invar alloys", Int. J. Adv. Manuf. Technol., 53 (9-12), 1049–1062.
12. Le Guen, E., Carin, M., Fabbro, R., Coste, F. and Le Masson, P. (2011); "3D heat transfer model of hybrid laser Nd:Yag-MAG welding of S3555 steel and experimental validation", Int. J. Heat Mass Tran., 54 (7/8), 1313–1322.
13. Xu, X. G., Wu, C. S., Qin, G. L., Wang, X. Y. and Lin, S. Y. (2011); "Numerical analysis of temperature profile and weld dimension in laser plus pulsed gas metal arc welding hybrid welding", J. of Eng. Manuf., 225 (B4), 528–542.
14. Xu, X. G., Wu, C. S., Qin, G. L., Wang, X. Y. and Lin, S. Y. (2011); "Adaptive volumetric heat source models for laser beam and laser plus pulsed GMAW hybrid welding processes", Int. J. Adv. Manuf. Technol., 57 (1-4), 244–255.
15. Piekarska, W. and Kubiak, M. (2013); "Modeling thermal phenomena in single laser and laser-arc hybrid welding processes using projection method", Appl. Math. Model., 37 (4), 2051–2062.
16. Piekarska, W. and Kubiak, M. (2011); "Three-dimensional model for numerical analysis of thermal phenomena in laser-arc hybrid welding processes", Int. J. Heat Mass Tran., 54 (23/24), 4966–4974.
17. Cho, J. H. and Na, S. J. (2009); "Three-dimensional analysis of molten pool in GMA-Laser hybrid welding", Weld. J., 88, 35–43.
18. Wu, C. S., Wang, H. G. and Zhang, Y. M. (2006); "A new heat source model for keyhole plasma arc welding in FEM analysis of temperature profile", Weld. J., 284s–291s.

APPENDIX-I

Commonly, hybrid welding employs a laser beam with high power density to facilitate deep penetration through the keyhole mode of welding. A keyhole of conical shape (XYZ) is considered here for simplicity as shown in **Fig. A1**. The keyhole is supported by a molten region of also conical shape (ABCD, truncated cone) as shown in **Fig. A1**. The total energy required to establish a conical keyhole of base radius r_v and height z_2 can be given as

$$q_k = \frac{1}{3}\pi\, r_v^2\, z_2\, \rho[C_{ps}(T_L - T_A) + L_m + C_{pl}(T_B - T_L) + L_v] \quad \text{(A1)}$$

where C_{ps} and C_{pl} are the average specific heats respectively in the solid and liquid states, L_m and L_v are the latent heats of respectively melting and vaporization, and T_L, T_B and T_A are the melting and boiling temperature of workpiece material and the ambient temperature, respectively. The energy required to support the molten region around the keyhole can be given as

$$q_m = V_m\, \rho[C_{ps}(T_L - T_A) + L_m] \quad \text{(A2)}$$

where V_m is the volume of the conical molten region (**Fig. A1**) and is estimated as

$$V_m = \frac{1}{3}\pi\, r_1^2\, z_2\left(1 + \frac{r_2}{r_1}\right) - \frac{\pi r_2^3 z_2}{3r_1} - \frac{\pi\, r_v^2\, z_2}{3} \quad \text{(A3)}$$

The beam energy facilitating the keyhole can be estimated as

$$Q_v = \int_0^{2\pi}\int_0^{r_v} \frac{3\eta_\ell P_\ell \tau}{\pi r_1^2} \exp\left[-3\frac{r^2}{r_1^2}\right] r\, dr\, d\theta = \eta_\ell P_\ell \tau\left[1 - \exp\left(3\frac{r_v^2}{r_1^2}\right)^{-1}\right] \quad \text{(A4)}$$

where τ is a presumed time duration. Similarly, the beam energy facilitating the molten region surrounding the keyhole can be estimated as

$$Q_m = \int_0^{2\pi}\int_{r_v}^{r_1} \frac{3\eta_\ell P_\ell \tau}{\pi r_1^2} \exp\left[-3\frac{r^2}{r_1^2}\right] r\, dr\, d\theta = \eta_\ell P_\ell \tau\left[\exp\left(3\frac{r_v^2}{r_1^2}\right)^{-1} - \frac{1}{e^3}\right] \quad \text{(A5)}$$

Equating (A1) and (A3), and (A2) and (A5), the values of r_v and z_2 can be estimated for a given beam power and focused beam radius (r_1) at the top surface of workpiece.

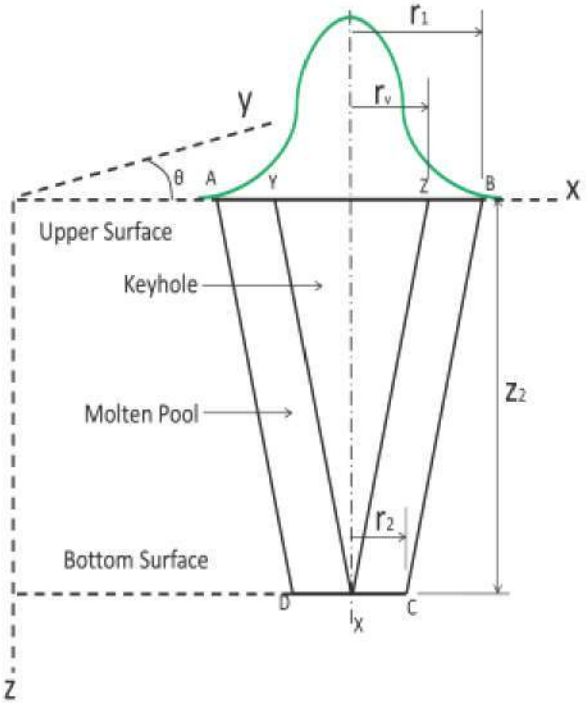

Fig. A1 : Schematic presentation of volumetric heat source .

Table 1 : Process parameters for laser-GTA hybrid welding of A131 and AISI 321 steel

Input Parameters		**A131 [2]**	**AISI321 [5]**
Thickness of the workpiece (mm)		10	4
Heat source separation distance (mm), Welding speed (mm/s)		3.0, 8.5	3.0, 16.67
Arc Source	Effective radius (r), Energy distribution factor (d)	2.0 mm, 1.0	2.0 mm, 1.0
	Efficiency (η), Current (A), Voltage (V)	0.75, 190, 12.3	0.75, 120, 12.0
Laser Source	Effective radius (r), Energy distribution factor (d)	0.5 mm, 3.0	0.5 mm, 3.0
	Efficiency (η), Power (W)	0.30, 4500	0.30, 1500
Emissivity (ε), Ambient Temperature (T_0)		0.8, 300 K	